REVIEW SUMMARY

BATTERIES

The nanoscale circuitry of battery electrodes

Changbao Zhu, Robert E. Usiskin, Yan Yu, Joachim Maier*

BACKGROUND: Developing high-performance, affordable, and durable batteries is one of the decisive technological tasks of our generation. Designing such batteries requires more than just the identification of electroactive storage materials with desirable properties such as high voltage, high capacity, and sufficient stability. These materials must also be assembled with ion- and electron-conducting phases into a composite electrode architecture, and this step is of equal significance; the size, shape, and spatial distribution of the various phases have a decisive influence on the charging and discharging rate capability of the electrode. Because the combined motion of ions and electrons within the solid is notoriously sluggish at room temperature, reduction of the transport length by downsizing the storage particles is indispensable. However, this necessity shifts the transport problems to the electrode's internal circuitry. That is, every electroactive particle must be part of a network that rapidly provides both ions from an electrolyte and electrons from an electronic current collector. If nanosized particles are used, then a myriad of particles and connections are required, resulting in a network with a degree of nanoscale intricacy comparable to that of electronic circuits in information technology or bioelectrochemical networks in living systems (see the figure). While electronic circuits are based on electron transport and bioelectrochemistry relies on ion motion, battery electrodes require a combination of electron-conducting, ion-conducting, and mixed-conducting phases.

ADVANCES: Criteria for rational electrode design are based on transport and dimensional parameters. The optimal size of the storage particles can be estimated from the chemical diffusivity and the (dis)charging rate needed in the application. An important strategy is to implement two different length scales over which ions and electrons must diffuse within the storage phase to reach the ionic (electrolyte) and electronic current collector phases. The optimal values of these two "wiring lengths" depend on the ionic and electronic conductivities of the storage material. Nanoscale structures with different dimensionalities such as dots, fibers, and sheets are often useful for various reasons. If the current-collecting phases exhibit appreciable resistance due to tiny feature sizes, a hierarchical structure is helpful. Such considerations help to optimize the morphology and simplify the circuitry. They also provide a conceptual framework for organizing the vast literature on nanostructured battery materials and for reviewing characteristic topologies in a systematic way. To realize the targeted electrode architectures, substantial progress has been achieved by adapting various chemical and physical preparation methods. The figure shows lithium-storing tin particles embedded in a 2-μm-diameter carbon fiber prepared by electrospinning. Often a synthesized structure must deviate from the general design criteria to address material-specific stability issues such as interfacial reactivity, crack formation, agglomeration, and dendrite growth. Structural evolution during battery cycling is being elucidated by new methods based on x-ray absorption, electron microscopy, and other nondestructive probes that can provide in operando analysis at a variety of length scales.

ON OUR WEBSITE

Read the full article at http://dx.doi.org/10.1126/science.aao2808

OUTLOOK: More powerful multiscale computational approaches are needed to adequately model the mixed-conducting electrode networks. Such numerical treatments will be helpful in optimizing electrode structures beyond the semiquantitative design rules reviewed here. The further development of synthetic methods is also vital, so that the desired complex and hierarchical architectures can be systematically reduced into practice. Whether or not even self-organized networks may be realized—as is the case in bioelectrochemical systems—remains to be seen. Finally, continued development of in operando characterization methods will surely boost our still-limited understanding of combined ion and electron transport in the presence of complicating factors such as mechanical strain, slow interfacial reactions, crystallographic anisotropy, phase transformations, and morphological instability. ■

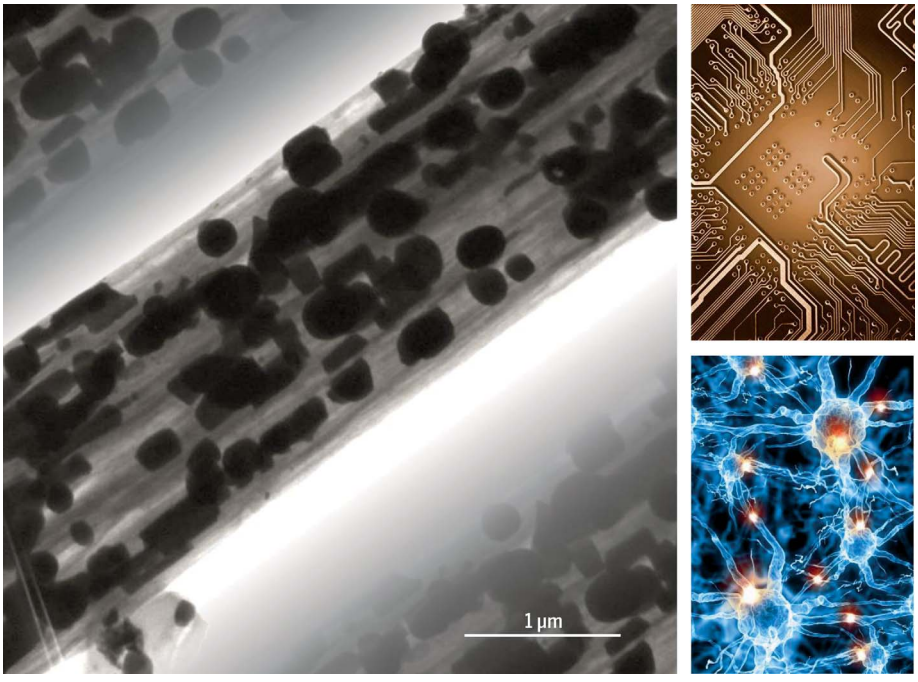

Battery electrodes, integrated electronic circuits, and bioelectrochemical networks all exhibiting intricate connections and nanoscale charge transport, although for different reasons.

The list of author affiliations is available in the full article online.
*Corresponding author. Email: weiglein@fkf.mpg.de
Cite this article as C. Zhu *et al.*, *Science* **358**, eaao2808 (2017). DOI: 10.1126/science.aao2808

REVIEW

BATTERIES

The nanoscale circuitry of battery electrodes

Changbao Zhu,[1]* Robert E. Usiskin,[1] Yan Yu,[1,2] Joachim Maier[1]†

Developing high-performance, affordable, and durable batteries is one of the decisive technological tasks of our generation. Here, we review recent progress in understanding how to optimally arrange the various necessary phases to form the nanoscale structure of a battery electrode. The discussion begins with design principles for optimizing electrode kinetics based on the transport parameters and dimensionality of the phases involved. These principles are then used to review and classify various nanostructured architectures that have been synthesized. Connections are drawn to the necessary fabrication methods, and results from in operando experiments are highlighted that give insight into how electrodes evolve during battery cycling.

The task of improving battery electrodes can be divided into two parts: the development of new materials and the assembly of these appropriately sized materials into a suitable architecture. The issue of materials exploration is described in various reviews (*1*–*3*), and the structural and chemical requirements are fairly well understood, to the point where computational tools have been developed to scan the compositional space (*4*). However, for the equally important issue of how to design the size, shape, and arrangement of the different phases in a composite electrode structure, there are only a few systematic treatments (*5*, *6*). This dearth underscores three important points: (i) the understanding of kinetics in such composite systems is not sufficiently developed; (ii) for many materials the decisive transport parameters are unmeasured or uncertain; and (iii) the issue is highly complex and involves multiple phases and length scales.

Despite these challenges, substantial conceptual and experimental progress has been made over the past two decades. Here, we review this progress in four parts. The discussion begins with principles for optimizing electrode kinetics based on the transport parameters and dimensionality of the phases involved. Next, these principles are used to review and classify some important recently developed nanostructured architectures. Connections are then drawn to the necessary fabrication methods, and the final section highlights recent results from in operando experiments that are providing insight into how the mixed-conducting network evolves during cycling.

This review focuses on lithium-storing electrodes, but the same concepts apply to electrodes based on sodium or other elements. For convenience, the electrolyte phase will sometimes be abbreviated by I (ionic current collector), the electron-providing phase by E (electronic current collector), and the lithium-storing active phase by M (mixed ionic and electronic conductor). The discussion will revolve mostly around single-phase storage (e.g., $LiCoO_2$)—the most well-defined and important storage mechanism—but reference will also be made to the three other possible mechanisms: storage by a phase transformation (e.g., in $FePO_4$–$LiFePO_4$), storage by a multiphase conversion reaction (e.g., Li_2S, FeF_3), and interfacial storage (e.g., as typically accompanies conversion reactions) (*7*).

[1]Max Planck Institute for Solid State Research, Heisenbergstrasse 1, 70569 Stuttgart, Germany. [2]Key Laboratory of Materials for Energy Conversion, University of Science and Technology of China, Hefei 230026, Anhui, P.R. China.
*Present address: Department of Materials Science and Engineering, Sun Yat-Sen University, Guangzhou 510275, Guangdong, P.R. China.
†Corresponding author. Email: weiglein@fkf.mpg.de

Principles of rational network design

The simplest electrode architecture consists of a single active particle and is shown schematically in Fig. 1A. If contact resistances are negligible and the I and E phases exhibit sufficiently high ionic and electronic conductivity, then the electrode kinetics are determined solely by solid state transport within the particle. This transport is characterized—notwithstanding implicit mechanical strain effects—by an intermingling of electrical migration and chemical diffusion. The governing classical transport equations essentially involve a local combination of Ohm's law and Fick's law [see, e.g., (*8*)]. If the geometry is quasi–one-dimensional (1D), analytical solutions can be derived (*9*–*11*), and the situation can be mapped to an equivalent electrical circuit (Fig. 1B) (*12*, *13*). Charge carrier interactions can be included (*14*). Typically M contacts I and E only on part of its surface, and in this general case, the propagation of formally neutral lithium depends on the ionic and electronic conductivities (σ_{ion} and σ_{eon}) of the active phase M. If $\sigma_{eon} >> \sigma_{ion}$, then lithium diffuses inward from the I/M interface; if $\sigma_{ion} >> \sigma_{eon}$, diffusion proceeds from the E/M interface; and if $\sigma_{ion} \sim \sigma_{eon}$, then lithium diffuses inward from both interfaces simultaneously (*9*). In all these cases, the relaxation time can be written as $\tau^{\delta} \sim L^2/D^{\delta}_{Li}$, where L is the particle radius or half-thickness and D^{δ}_{Li} the effective chemical diffusivity of neutral lithium (Li^+ and e^-) in phase M (*10*). This relaxation time can also be expressed from an electrical perspective as $\tau^{\delta} \sim R^{\delta}C^{\delta}$, where R^{δ} is a transport resistance that depends on the arithmetic mean of the ionic and electronic resistances (Fig. 1B) and C^{δ} is a chemical capacitance that depends in ideal cases on the harmonic mean of the ionic and electronic carrier concentrations. See (*13*) for details.

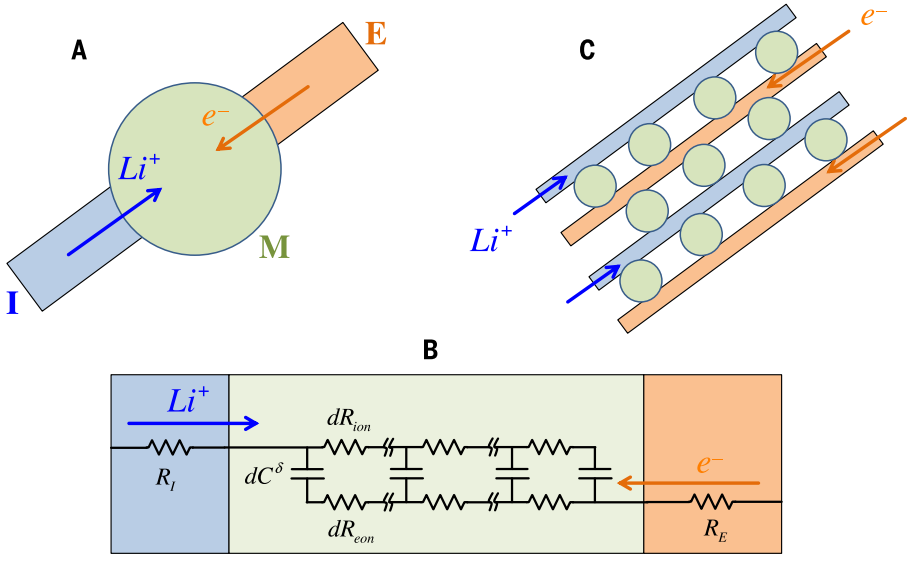

Fig. 1. Transport in a battery electrode. (**A**) Schematic of Li^+ and e^- diffusion through an ion conductor I (blue) and an electron conductor E (orange) into a mixed-conducting storage particle M (green). (**B**) Equivalent electrical circuit for the contact geometry shown in (A) using a quasi-1D approximation. (**C**) Transport into a many-particle network.

Table 1 lists D^{δ}_{Li} values obtained in the literature for selected anodes and cathodes at 25°C. It is noteworthy that reliable data on transport properties are rather scarce; nonetheless, it is clear that the values are fairly low. The only exception (and so far the upper limit for solid-state lithium diffusivity at room temperature) is for transport within a graphene bilayer (*15*). As a result, fully lithiating a large, dense particle takes an impractical amount of time—e.g., ~14 weeks for a 1- mm-thick sheet with D^{δ}_{Li} = 10^{-8} cm^2/s. Apart from a few exceptions, chemical diffusion is expected to be no higher in sodium-storing materials and substantially slower in magnesium-storing materials. Silver chalcogenides allow for fast chemical diffusion of Ag (*16*), but they are not serious candidates for battery applications. In short, architectures using a single dense particle are only practical in applications requiring very low capacity or power (e.g., thin-film batteries for miniature electronic devices).

For all other applications, the common strategy is to break up the large, dense monolith into many smaller particles (Fig. 1C). Owing to the quadratic dependence of τ^{δ} on L, the effect of reducing L can be immense: A reduction from 1 mm to 10 nm corresponds to a reduction of storage time by 10 orders of magnitude. A striking example is rutile TiO_2, which was long assumed to be unable to host Li, but downsizing to 10 nm showed that this apparent behavior was a kinetic artifact, and that in fact, the thermodynamic storage capacity of rutile TiO_2 is comparable to anatase TiO_2 (*17*). Indeed, at first glance, downsizing may seem sufficient in all cases except for extremely low D^{δ} values ($<10^{-18}$ cm^2/s), where the necessary particle size becomes unrealistic ($<$ 1Å for a charging time of 1 hour). Yet a new problem arises: The particle volume scales with L^3, so as L enters the nanoscale, the number of particles needed to maintain the same capacity becomes enormous. In the above example of size reduction from 1 mm to 10 nm, the number of particles increases by a factor of 10^{15}, and all of them must be efficiently supplied with ions and electrons to take advantage of the size effect on transport time. Hence, the difficulty of providing a mixed conductor with high D^{δ} is shifted to the difficulty of constructing a percolating, effectively mixed-conducting network.

Because downsizing the storage particles can introduce a multitude of other problems (discussed more systematically below), a natural strategy is to aim for the largest particle size that allows for complete (dis)charging in the smallest time (fastest rate) needed in the desired application. Often, battery engineers use the term "C rate," defined such that at a C rate of "n," the battery can be fully (dis)charged in $1/n$ hours. We will refer to the smallest needed (dis)charge time (which is approximately the reciprocal of the fastest needed C rate) as τ^*. The corresponding particle radius or half-thickness L^* can be written as:

$$L^* = \sqrt{\alpha D^{\delta} \tau^*} \qquad (1)$$

The constant α is hardly influenced by materials parameters to a first approximation, but it does depend on geometry and charging mode—i.e., whether the current or voltage is controlled. For example, when filling a platelet-shaped particle supplied with both ions and electrons over the entire surface to 99% of its theoretical capacity, α equals 0.03 under constant current (*18*) and 0.56 under constant voltage (*10*); for a spherical particle, the corresponding values are 0.15 and 2.40. Considering Fig. 1C, we can—for the simplified situation considered so far—formulate the following "wiring rules" for designing the network: The I and E phases should be continuous and percolating, whereas percolation of M is not necessary. The M particles should have a half-thickness of approximately L^*. In other words, the active phase should be embedded in a bicontinuous network that is effectively mixed-conducting (continuous for I and E) but heterogeneous on the order of L^* (*19*).

In electrodes of practical importance, the transport geometry is higher dimensional and more complicated. In particular, the two distances ("wiring lengths") that ions and electrons must diffuse within the active phase to reach the I and E contact phases are often very different, due to different contact geometry. Indeed, because σ_{ion} and σ_{eon} in the M particle often differ by orders of magnitude, one would expect that the optimal values for these distances, L^*_{ion} and L^*_{eon}, will also be different. (It can be shown that in typical cases, the optimal wiring lengths are given by $L^*_{ion} \sim L^*/\sqrt{t_{eon}}$ and $L^*_{eon} \sim L^*/\sqrt{t_{ion}}$, where $t_{eon} = \sigma_{eon} / (\sigma_{eon} + \sigma_{ion})$ and $t_{ion} = 1 - t_{eon}$ are the electronic and ionic transference numbers).

This strategy of designing the wiring lengths based on the ionic and electronic conductivities takes maximum advantage of the transport capabilities of the particle. Unnecessary nanoheterogeneity is thereby avoided, which mitigates a number of problems that can arise at the nanoscale. For instance, implementing the same wiring length for both ions and electrons can require a larger amount of inactive I and E contact phases, which decrease the gravimetric and volumetric energy density of the electrode. The contact phases may also compete with each other. A direct blocking effect is possible; for example, coating an M particle with an E phase will block ions unless the E coating has porosity or some ionic conductivity. The competition can also be a matter of wetting, either as a consequence of modified surface tension or worsened contact geometry [cf. Lotus effect (*20*)]; for example, introducing graphite into the network could worsen the local wettability of the active particles by the electrolyte as a consequence of local chemical repulsion or the generated geometrical intricacy (in terms of area to be wetted and/or wetting angles). The higher surface-area-to-volume ratio may lead to increased interfacial reactivity [formation of a solid-electrolyte interphase (SEI)], tendency for agglomeration, or impurity content. Decreased particle size yields a different chemical potential of Li and hence a modified cell potential and increased solubility (*7*, *21*). Decreased pore sizes may lead to increased concentration polarization in the electrolyte and even to salt precipitation. Finally, unnecessary reduction of the wiring lengths will typically increase the synthesis complexity and cost. In short, one is well advised not to implement wiring lengths below the optimal values without good reason. A refined wiring rule is needed: The M particle should be shaped and contacted by the I and E phases such that the wiring lengths for ions and electrons are as close to L^*_{ion} and L^*_{eon} as is practically feasible. In other words, a bicontinuous mixed-conducting network is desired with different heterogeneity scales for the ionic and electronic current collecting phases.

Several notes on the applicability of the wiring rules are warranted. First, the transport rates (and thus the optimal length scales) can change during cycling. Grain boundaries can introduce additional resistances or fast paths for diffusion, so it is important to include them in the computation of L^* (*14*). Anisotropic transport may introduce additional complexity (*22*). For materials that store lithium by a phase transformation, the optimal lengths will depend in part on the properties of the new phase. The same is true for storage by a conversion reaction, and often the conversion products exhibit such slow transport that the necessary wiring lengths become tiny. On the other hand, conversion creates a high density of interfaces that can boost storage. See (*23*) for further discussion of this point. The contacts with the E and I phases may not be ideal; lower L^* values must be invoked in less ideal cases such as point contacts [cf. (*24*)]. In the extreme case where surface exchange is rate-limiting instead of bulk diffusion, Eq. 1 must be replaced by a linear relation of L^* versus τ^* and D^{δ} replaced by a surface rate constant.

Table 1. Effective chemical diffusivity of neutral lithium in various materials at 25°C. Values shown are estimates.

	D^{δ}_{Li} / cm^2 s^{-1}	Source
Cathode materials		
$LiFePO_4$	10^{-13}	(*98*)*
$LiMn_2O_4$	10^{-11} to 10^{-9}	(*99*)
$LiCoO_2$	10^{-10} to 10^{-8}	(*99*)
$LiNi_{0.5}Mn_{1.5}O_4$	10^{-9}	(*100*)
$LiNi_{0.8}Co_{0.2}O_2$	10^{-8}	(*101*)
Anode materials		
Li_xWO_3 film	10^{-12} to 10^{-11}	(*102*)
Li_xSnSb	10^{-12} to 10^{-10}	(*103*)
Li_xC_6	10^{-12} to 10^{-7}	(*104*)
Li_2MoO_3, $Li_4Mo_5O_{12}$	10^{-10} to 10^{-8}	(*105*)
Li_xSn	10^{-8} to 10^{-7}	(*106*)
Bilayer graphene	10^{-5} to 10^{-4}	(*15*)

*Value shown for $LiFePO_4$ is estimated from a sample with antisite defects blocking the fast b-direction channels. Samples with unblocked channels may exhibit higher D^{δ}_{Li}.

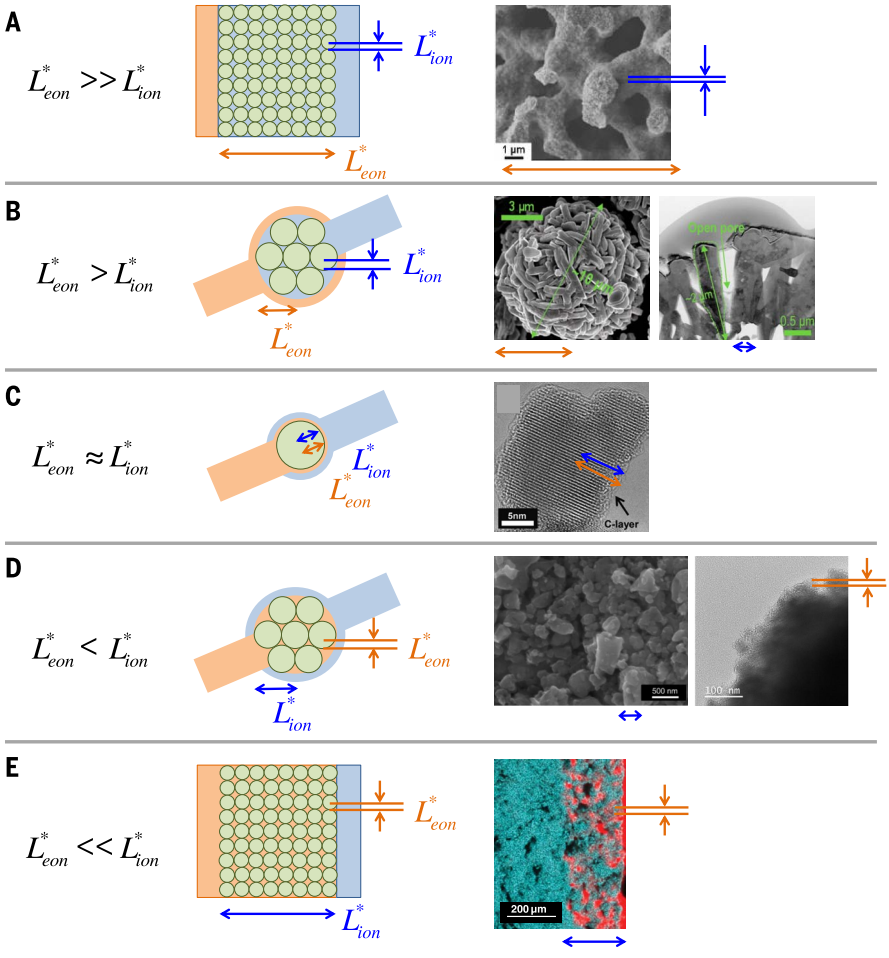

Fig. 2. Strategies for connecting a network of storage particles. A schematic and a practical example are shown for each case. (**A**) $L^*_{eon} \gg L^*_{ion}$, porous C monolith anode (*27*). (**B**) $L^*_{eon} > L^*_{ion}$, Li_2MnO_3 – $LiNi_{0.5}Mn_{0.5}O_2$ – C cathode (*28*). (**C**) $L^*_{eon} \approx L^*_{ion}$, $LiMn_2O_4$ – C cathode (*29*). (**D**) $L^*_{eon} < L^*_{ion}$, $Na_3V_2(PO_4)_3$ – C sodium cathode (*30*). (**E**) $L^*_{eon} \ll L^*_{ion}$, $Li_{10}GeP_2S_{12}$ – C electrode (displayed in green-red false color) (*31*). Micrographs are reproduced with permission from the indicated sources.

Although the conductivities of the I and E phases are typically high, transport in those networks can nevertheless be an additional limiting factor if the design requires thin features that extend over substantial distances. In such cases, a hierarchical structure becomes useful. For larger L^*_{ion} or L^*_{eon} values and sufficient conductivity, the electroactive particles can assist in the percolation of the I or E networks as either a connector in series or an additional current path in parallel. [For an example of a tricontinuous network, see (*25*)]. An important special case is faced if L^*_{ion} or L^*_{eon} is larger than the overall electrode size; then the I or E phase is not needed at all, leading to an enormous simplification of the architecture.

Before discussing and reviewing electrode architectures from the literature, it is useful to address the impact of dimensionality in terms of wiring length, percolation, and volumetric density. For a 3D monolith, the latter two parameters are trivially perfect, but diffusion is sluggish if all three dimensions are macroscopic. For that reason, it is essentially the I and E phases outside the electrode compartments that are 3D objects. If one parameter is already nanoscopic, diffusion is much quicker. Rapid diffusion is particularly pronounced for nanoparticles ("0D" objects), so they are excellent candidates for electroactive phases with low D^δ. The poor connectivity of 0D objects is not problematic here, because percolation of the storage phase is not needed. One-dimensional objects have the advantage that for mechanical reasons the macroscopic length can often be substantial, and hence needle-like structures are rather easy to obtain in many cases. As the percolation threshold for rigid rodlike objects decreases with increasing aspect ratio (*26*), 1D objects are well suited as electronic current collectors. The applicability of 2D objects (i.e., sheets) depends very much on the arrangement, the mechanical properties, and the application. For thin-film batteries, they can serve as E, I, and M phases; in nanostructured batteries, graphene envelopes can serve as efficient and volume-saving current collectors. These remarks on dimensionality are greatly simplified and deserve refinement, in particular when porous and hierarchical structures are involved.

Archetypal architectures

The parameters L^*_{eon} and L^*_{ion} refer to the optimal length scales over which ions and electrons must diffuse within the active phase to reach the contact phases. A simple case is realized if the active phase is a very good electronic conductor such as a metal or carbon, so that $L^*_{eon} \gg L^*_{ion}$. Then the I network must contact the electroactive mass on a fine scale, whereas the E phase can be made much coarser or completely dispensed with in the electrode architecture. Figure 2A shows the situation both schematically and for the practical example of a high-performance hierarchical porous carbon monolith (*27*). The hierarchical pore size distribution allows the liquid electrolyte to penetrate and thus the ions to quickly reach the electroactive particles on a mesoporous length scale, and because of the high electronic conductivity of the M phase, admixing an additional electronic current collector is not necessary.

The situation where $L^*_{eon} > L^*_{ion}$ is shown in Fig. 2B. Both electron- and ion-collecting phases must be included, but the electron-collecting network can be much coarser. In the example shown, the electroactive material is the predominantly electron-conducting composite Li_2MnO_3: $LiNi_{0.5}Mn_{0.5}O_2$ (*28*). It suffices to contact each ~10-µm agglomerate with the carbon network (left micrograph), whereas more intricate sub-100-nm pores are needed to allow the electrolyte to penetrate (right micrograph).

Figure 2C refers to the case where σ_{ion} and σ_{eon} (and hence L^*_{ion} and L^*_{eon}) are comparable. The example shown is $LiMn_2O_4$ (*29*); here, the particles are contacted by carbon and liquid electrolyte on the same ~20-nm-length scale.

Figure 2D addresses the situation in which L^*_{ion} is substantially larger than L^*_{eon} but still smaller than the overall electrode size. Such a case is met in the sodium storage material $Na_3V_2(PO_4)_3$, which takes the NASICON structure and hence is a fairly good Na^+ conductor. As demonstrated in (*30*), it suffices to coat the $Na_3V_2(PO_4)_3$ particles with polymer electrolyte on a ~1-µm scale (Fig. 2D, left micrograph) rather than penetrating to the ~10-nm scale at which the carbon coating is observed (right micrograph).

The extreme case of an electroactive phase with much higher ionic than electronic conductivity is shown in Fig. 2E. The example refers to the superionic conductor $Li_{10}GeP_2S_{12}$ (*31*), a solid electrolyte with Li^+ conductivity of ~10^{-2} S/cm. This phase does not allow for a perceptible solubility of lithium owing to the high energy of electronic defects, so the electroactivity relies on a conversion reaction. The conversion products exhibit much slower ion transport, and thus the rate capability is modest. Nevertheless, the example is pertinent because it illustrates a case in which the only added phase is an electron conductor.

In many cases, one must deviate from the otherwise optimal wiring lengths to solve specific problems that arise in practice. One common

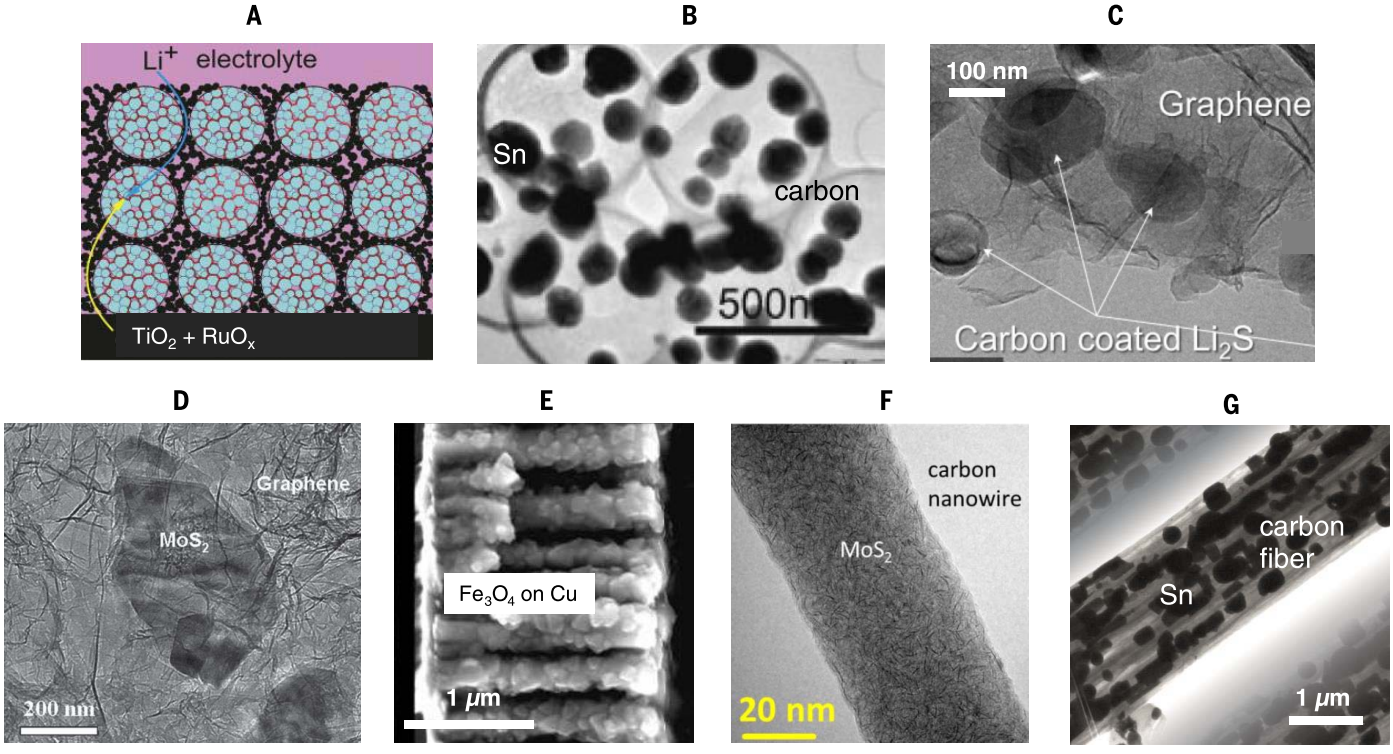

Fig. 3. Electrode architectures with various dimensionalities. An electron micrograph or a schematic is shown for each. (**A**) Hierarchical network of TiO_2, carbon, and RuO_2 (*33*). (**B**) Sn particles inside carbon shells (*35*). (**C**) Carbon-coated Li_2S nanoparticles on graphene (*39*). (**D**) MoS_2 nanosheets mixed with graphene flakes (*40*). (**E**) Fe_3O_4-coated Cu nanowires (*41*). (**F**) Single-layer MoS_2 nanodots embedded in carbon nanowires (*42*); (**G**) Sn particles embedded in porous carbon fibers (*43*). Micrographs are reproduced with permission from the indicated sources.

problem is morphological instability due to cracking of the storage phase. For example, high-capacity metals such as Sn would ideally be implemented as shown in Fig. 2A to take advantage of the high electronic conductivity. However, the severe volume change upon lithiation typically causes cracking, pulverization, and loss of connectivity. A better solution is then to begin with small, isolated active particles admixed with a percolating electron-collecting phase, as in Fig. 2C. An intended morphology may also be unstable due to agglomeration effects during synthesis or operation. For instance, the primary benefit of adding a carbon coating to $LiFePO_4$ particles is typically inhibited agglomeration rather than a smaller electronic wiring length (*32*).

Additional examples characterized by a variety of dimensionalities, percolation schemes, and storage mechanisms for the M and E phases are shown in Fig. 3. For instance, a very effective mixed-conducting network based on anatase TiO_2 is shown in Fig. 3A (*33*); it uses a hierarchical approach. On a 100-nm scale, the TiO_2 aggregates are contacted by both carbon and electrolyte-filled pores. On a 3-nm scale within the agglomerates, individual particles are contacted by both electron-conducting RuO_x and electrolyte-filled mesopores. The resulting structure yields substantially higher capacities than 5-nm anatase particles at ≥10C charging rates, whereas at lower rates the capacities are comparable. A similar hierarchical design was used for $LiFePO_4$ in (*34*).

An elegant structure that buffers volume changes while providing reasonably good packing is the "yolk-shell" solution for Sn shown in Fig. 3B (*35*). Such a structure has also been implemented for Si (*36*). In both these examples, additional carbon is used to electronically interconnect the shells. Hollow concentric tubes may be even better in the sense that they can accommodate the volume expansion without loss of percolation, such that additional carbon may not be necessary (*37*). There is also evidence that SEI growth can be suppressed by a concentric arrangement that shields a susceptible phase from direct contact with the electrolyte (*38*). To maintain good electronic percolation, graphene can be favorably used (Fig. 3, C and D) (*39*, *40*). An example of implementing a conversion reaction that demands short wiring lengths for both ions and electrons is shown in Fig. 3E. Here, 1D copper pillars are coated with Fe_3O_4 (*41*), which converts upon lithiation to Li_2O and Fe. An even more pronounced reaction confinement is achieved by the architecture in Fig. 3F. In this case MoS_2 "nanodots" are embedded with fairly high volume fraction in nanoscale carbon fibers (*42*). These nanodots are single-molecular in one dimension (0.4 nm) and less than 4 nm in the other dimensions. Consequently, the reaction products are confined to a volume less than 10 nm^3, and the conversion is extraordinarily reversible. Size effects also reduce the voltage versus Li by a few hundred mV, which is beneficial for the role of this structure as a negative electrode.

In Fig. 3G, we highlight a final example that shows how the above considerations can be brought together to yield an architecture with very fast kinetics. Here, 250-nm particles of Sn are embedded in 2-μm carbon microtubes soaked in a liquid electrolyte (*43*). As in the MoS_2 example, the resulting "(0D–M ⊂ 1D–E) @ 3D–I" (*19*) structure illustrates the favorable use of different dimensionalities, and it approaches an optimized architecture that both complies with the general wiring rules and favorably addresses several specific problems. A list of the resulting advantages is instructive: (i) short diffusion pathways are achieved for both ions and electrons (the problem of cracking is mitigated by making the wiring length for electrons far smaller than the otherwise optimal value for Sn); (ii) the embedded configuration helps to maintain contact with the carbon during lithiation (further addressing the effects of volume expansion and cracking); (iii) both the electron collector (carbon) and ion collector (electrolyte) phases achieve good percolation, in part because the 1D fibers interweave during synthesis; (iv) the active particles are isolated from each other, with the consequence that Ostwald ripening does not take place (as the metal ions are not mobile within the carbon); (v) the embedded particles are partly shielded from direct contact with the electrolyte, so SEI formation is expected to occur primarily on the carbon/electrolyte interface; (vi) such structures could also be well suited for use with solid electrolytes, because the fiber porosity

should allow volume expansion to proceed inward, thus minimizing expansion effects at the carbon fiber/electrolyte interface; and (vii) the volume and mass fraction required for carbon are not totally lost in terms of storage; although primarily acting as a current collector, carbon is also electroactive for storage at low potentials.

Space constraints prevent a full review (*5*, *6*, *44*) of the numerous outstanding architectures that have been fabricated in recent years, in particular those that make favorable use of 0D (*45*), 1D (*46*–*49*), 2D (*50*–*54*), or 3D (*55*–*61*) dimensionality for the storage material.

Synthesis of the nanoscale architecture

Unlike integrated circuits or biological networks, intricate battery electrodes cannot (yet) rely on lithography or self-organization; other tailored, typically self-assembling approaches are needed. Detailed synthetic strategies have been reviewed elsewhere (*6*), but it is worth mentioning a few points. Broadly speaking, the strategies may be divided into the categories shown in Table 2. Solid-state synthesis is not the best method to realize a refined nanocircuitry, but it can be implemented at large scale and thus has had an enormous impact on the battery industry. Liquid-phase approaches such as (hydro)solvothermal synthesis (*62*) and template methods (*63*) are more fruitful for preparing nanostructures, and often the size and shape can be tuned by varying the precursors, surfactants, templates, and processing parameters.

Although there is no 1:1 correlation between synthesis method and network architecture, there are connections between the various synthesis methods and the resulting dimensionalities. For instance, exfoliation methods are excellent for preparing single-layer or multilayer 2D sheets of compounds with a layered crystal structure (*64*). Electrospinning is a widely used and effective technique for fabricating nanowires, micron-scale tubes, and even concentric 1D structures (*42*, *43*, *65*, *66*). Electrospray deposition is a related method for synthesizing porous 3D structures; it can achieve the smallest droplet sizes of all spray techniques. Both electrospinning and electrospraying can be performed at ambient pressure, and the resulting electrodes may need no added binder (*25*, *37*, *67*, *68*). Vapor deposition methods are generally restricted to thin-film applications, but barrier coatings are also being explored. One such method, atomic layer deposition, has the ability to grow a conformal coating with atomic accuracy on virtually any structure, regardless of intricacy and aspect ratio (*69*, *70*).

In operando characterization

In operando measurements are invaluable for understanding changes in the transport parameters or topology during cycling, as these measurements offer nondestructive, real-time, and nonequilibrium insights into the (dis)charging process, while avoiding the possible contamination associated with disassembling a battery for ex situ measurements (*71*, *72*). A large number of techniques have been successfully implemented during battery cycling (Fig. 4A) (*73*–*80*) to provide time-dependent information about electrochemical, chemical, and mechanical changes in electrodes. These changes may include one or more of the following: phase transformations; interfacial reactivity that creates contact resistances; formation and motion of point and line defects; expansion-induced mechanical stresses; crack formation and the associated loss of connectivity; gas evolution; agglomeration; and dendrite growth.

In terms of materials chemistry, one master example is the investigation of Li_xFePO_4, a model system for studying lithium storage by a phase transformation. The formation of a metastable solid solution in sub-200-nm Li_xFePO_4 particles when cycled at a sufficiently fast rate has now been observed in operando by x-ray diffraction (XRD) (*81*–*83*), scanning transmission x-ray microscopy (STXM) (*84*), and transmission electron microscopy (TEM) (*85*). The properties of such a phase may be difficult to capture by ex situ experiments, but using in operando STXM, it is even possible to measure the local surface exchange current in the metastable state (*84*). Intermediate phases, valence changes, and the associated diffusion behavior during lithiation of Si, VS_4, $Na_3V_2(PO_4)_2F_3$, Nb_2O_5, and other compounds have been probed by nuclear magnetic resonance (NMR) (*86*). The rate and pathway of diffusion may also be influenced by phase transformation dynamics. Bragg coherent diffraction imaging (BCDI) was used to map atomic-scale strains and dislocation dynamics during cycling of $LiNi_{0.5}Mn_{1.5}O_4$, and the results suggested that dislocations may act as nucleation sites for the phase transformation (*87*).

For monitoring phase topology and architecture changes during cycling, x-ray techniques are particularly versatile, because they can provide 2D and even 3D information at length scales from nm to mm. For example, STXM has demonstrated that phase boundary propagation in $LiFePO_4$ is strongly influenced by mechanical strain effects. Filaments of the transformed ($FePO_4$) phase were observed, and eventually crack formation occurred between the filaments (*88*). The filament spacing was ~200 nm, strikingly similar to the particle size of $LiFePO_4$ typically used commercially. STXM results have also shown that the fraction of particles undergoing (de)lithiation at any given instant during cycling can be as low as 2 to 10% (*89*). This low fraction is attributed not to differences in wiring of the I and E phases but rather to an energy barrier in the phase transformation that favors particle-by-particle lithiation at low charging rates. Crack formation can be studied by x-ray tomographic microscopy. Figure 4C shows the morphology of a SnO particle investigated with a resolution of 2 μm (*90*). The conversion of ~30-μm SnO particles into Li_2O and Li_xSn was observed to initially proceed in core-shell fashion consistent with diffusion-limited behavior, but before conversion was completed, cracks formed at grain

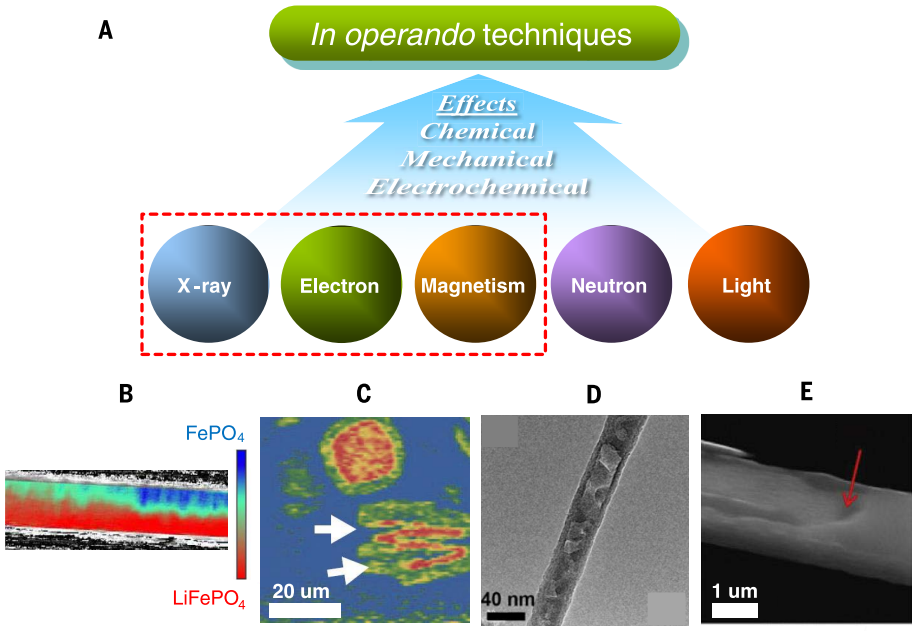

Fig. 4. In operando techniques in battery research. (**A**) Overview. Studies of architecture evolution generally address the categories within the dashed rectangle. (**B**) Filament-like diffusion profiles in $LiFePO_4$ (shown here in false color) observed by scanning transmission x-ray microscopy (*88*). (**C**) Core-shell diffusion and crack nucleation seen by x-ray tomographic microscopy of SnO particles (*90*). (**D**) Transmission electron micrograph of Si nanoparticles undergoing lithiation while embedded in carbon nanotubes (*95*). (**E**) Scanning electron micrograph of the diffusion front in a V_2O_5 nanowire (*96*). Images (B) to (E) are reproduced with permission from the indicated sources.

Table 2. Methods for fabricating nanoscale architectures.

Type of synthesis	Method	Possible dimensionality	Advantages
Solid state	Ball milling	0D, agglomerates	Feasible for large-scale applications
Liquid phase	Hydrothermal	0D, 1D, 2D, 3D porous	Controllable for various nanostructures
	Solvothermal	0D, 1D, 2D, 3D porous	
	Microemulsion	0D, 1D	
	Precipitation	0D, 3D	
	Sol-gel	0D, 3D porous	
	Template	0D, 1D, 2D, 3D porous	
	Spray drying	3D porous	Powerful for 3D porous structures
Field-assisted	Electrospinning	1D	Powerful for 1D structures
	Electrospraying	2D, 3D porous	Powerful for porous nanostructures
	Microwave-assisted synthesis	0D, 1D, 2D, 3D porous	High reaction rates
	Galvanic replacement synthesis	0D, 1D, 2D, 3D porous	Template morphology can be tailored
	Electrodeposition	0D, 2D	Effective for coatings and thin films
Vapor deposition	Chemical vapor deposition	0D, 2D	
	Physical vapor deposition	0D, 2D	
Exfoliation	Various	2D	Powerful for materials with a layered crystal structure

boundaries that were present preferentially in (001) planes, leading to electrolyte penetration in the cracks, distortion of the core-shell behavior, and particle breakup. These results provide further evidence that for reversible storage by a phase transformation or a conversion reaction, downsizing to the nanoscale may be necessary not just to compensate for slow diffusivity but also to avoid deleterious cracking. Tomography with hard x-rays can also nondestructively visualize the phase distribution on a μm or mm scale. For example, the gas bubbles that are generated by electrolyte decomposition during cycling can be mapped in 3D, thus providing spatial information about SEI formation and pressure buildup (*91*). Nonuniformities resulting from the fabrication can also be identified; for example, smaller particles may pack preferentially at the edges of an electrode (*92*). Tomography can be combined with x-ray absorption to yield a full 3D map of the lithium diffusion front with a resolution of ~150 nm (*93*).

Electron microscopy is also yielding important insights. A pioneering study using TEM observed the absence of crack formation while lithiating a single-crystal SnO_2 nanowire, in stark contrast to the polycrystalline SnO study described above. Instead, a high concentration of dislocations formed at the lithiation front, and the wire underwent considerable plastic deformation (*94*). In another TEM study, a confinement effect was suggested during the lithiation of Si nanoparticles embedded in carbon nanotubes (Fig. 4D). The formation of a Li-Si alloy resulted in pronounced (~180%) volume expansion, as expected, but crack formation and crumbling appeared to be reduced by the nanotube confinement, thus helping the structure to remain intact during battery operation (*95*). Scanning electron microscopy (SEM) can also be adapted to monitor morphology variations such as expansion and fracture during electrode cycling. For example, lithium propagation in an individual V_2O_5 nanowire has been tracked (Fig. 4E) (*96*).

Interestingly, resonance methods can be used to monitor dendrite growth during cycling. Specifically, both ^{7}Li nuclear magnetic resonance (NMR) (*97*) and electron paramagnetic resonance (EPR) (*74*) can distinguish between smooth deposition and rough dendrite formation in the early stages of Li metal plating on an anode. In the later stages, magnetic resonance imaging (MRI) can track the growth of Li metal microstructures with a spatial resolution of ~100 um (*75*). These capabilities could plausibly enable faster and more detailed evaluation of additives or architectures intended to control dendrite growth.

Conclusion

Although the limits of theoretical energy density based on the available mechanisms and materials space are in sight, substantial improvements in power density are still possible. Because solid-state transport in the electroactive masses is sluggish, nanotechnological solutions are required. The design principles reviewed above provide a conceptual framework for tailoring the complex electrochemical circuitry in principle, and advanced preparation and in operando characterization methods are indispensable for optimizing the electrodes in practice.

REFERENCES AND NOTES

1. B. Dunn, H. Kamath, J.-M. Tarascon, Electrical energy storage for the grid: A battery of choices. *Science* **334**, 928–935 (2011). doi: 10.1126/science.1212741; pmid: 22096188
2. P. G. Bruce, B. Scrosati, J. M. Tarascon, Nanomaterials for rechargeable lithium batteries. *Angew. Chem. Int. Ed.* **47**, 2930–2946 (2008). doi: 10.1002/anie.200702505; pmid: 18338357
3. N. S. Choi *et al.*, Challenges facing lithium batteries and electrical double-layer capacitors. *Angew. Chem. Int. Ed.* **51**, 9994–10024 (2012). doi: 10.1002/anie.201201429; pmid: 22965900
4. M. S. Islam, C. A. J. Fisher, Lithium and sodium battery cathode materials: Computational insights into voltage, diffusion and nanostructural properties. *Chem. Soc. Rev.* **43**, 185–204 (2014). doi: 10.1039/C3CS60199D; pmid: 24202440
5. J. W. Long, B. Dunn, D. R. Rolison, H. S. White, Three-dimensional battery architectures. *Chem. Rev.* **104**, 4463–4492 (2004). doi: 10.1021/cr020740l; pmid: 15669159
6. A. Vu, Y. Q. Qian, A. Stein, Porous electrode materials for lithium-ion batteries - How to prepare them and what makes them special. *Adv. Energy Mater.* **2**, 1056–1085 (2012). doi: 10.1002/aenm.201200320
7. J. Maier, Thermodynamics of electrochemical lithium storage. *Angew. Chem. Int. Ed.* **52**, 4998–5026 (2013). doi: 10.1002/anie.201205569; pmid: 23630067
8. H. Rickert, in *Electrochemistry of Solids: An Introduction*, H. Rickert, Ed. (Springer, Berlin, Heidelberg, 1982), pp. 79–117.
9. W. Preis, W. Sitte, Theory of galvanostatic processes in mixed conductors with arbitrary electronic transport numbers. *J. Chem. Soc., Faraday Trans.* **92**, 1197–1203 (1996). doi: 10.1039/ft9969201197
10. J. Crank, *The Mathematics of Diffusion* (Clarendon Press, Oxford, England, 1975).
11. W. Preis, Non-Cottrell behaviour of potentiostatic processes in mixed conductors with comparable ionic and electronic conductivities. *Ber. Bunsenges. Phys. Chem* **101**, 50–58 (1997). doi: 10.1002/bbpc.19971010106
12. W. Lai, F. Ciucci, Small-signal apparent diffusion impedance of intercalation battery electrodes. *J. Electrochem. Soc.* **158**, A115–A121 (2011). doi: 10.1149/1.3515896
13. J. Jamnik, J. Maier, Generalised equivalent circuits for mass and charge transport: Chemical capacitance and its implications. *Phys. Chem. Chem. Phys.* **3**, 1668–1678 (2001). doi: 10.1039/b100180i
14. J. Maier, *Physical Chemistry of Ionic Materials: Ions and Electrons in Solids* (Wiley, 2004).
15. M. Kühne *et al.*, Ultrafast lithium diffusion in bilayer graphene. *Nat. Nanotechnol.* **12**, 895–900 (2017). doi: 10.1038/nnano.2017.108; pmid: 28581509
16. H. Schmalzried, Ag_2S–The physical chemistry of an inorganic material. *Prog. Solid State Chem.* **13**, 119–157 (1980). doi: 10.1016/0079-6786(80)90002-3
17. Y. S. Hu, L. Kienle, Y. G. Guo, J. Maier, High lithium electroactivity of nanometer-sized rutile TiO_2. *Adv. Mater.* **18**, 1421–1426 (2006). doi: 10.1002/adma.200502723
18. S. Atlung, K. West, T. Jacobsen, Dynamic aspects of solid-solution cathodes for electrochemical power sources. *J. Electrochem. Soc.* **126**, 1311–1321 (1979). doi: 10.1149/1.2129269
19. J. Maier, Control parameters for electrochemically relevant materials: The significance of size and complexity. *Faraday Discuss.* **176**, 17–29 (2014). doi: 10.1039/C4FD00135D; pmid: 25469595

20. A. Marmur, From hygrophilic to superhygrophobic: Theoretical conditions for making high-contact-angle surfaces from low-contact-angle materials. *Langmuir* **24**, 7573–7579 (2008). doi: 10.1021/la800304r; pmid: 18543997
21. C. Zhu *et al*., Lithium potential variations for metastable materials: Case study of nanocrystalline and amorphous $LiFePO_4$. *Nano Lett.* **14**, 5342–5349 (2014). doi: 10.1021/nl5024063 pmid: 25133677
22. G. K. Singh, G. Ceder, M. Z. Bazant, Intercalation dynamics in rechargeable battery materials: General theory and phase-transformation waves in LiFePO4. *Electrochim. Acta* **53**, 7599–7613 (2008). doi: 10.1016/j.electacta.2008.03.083
23. J. Maier, Pushing nanoionics to the limits: Charge carrier chemistry in extremely small systems. *Chem. Mater.* **26**, 348–360 (2014). doi: 10.1021/cm4021657
24. M. Gaberscek, J. Jamnik, Impact of electrochemical wiring topology on the kinetics of insertion electrodes. *Solid State Ion.* **177**, 2647–2651 (2006). doi: 10.1016/j.ssi.2006.02.035
25. C. Zhu, P. Kopold, P. A. van Aken, J. Maier, Y. Yu, High power-high energy sodium battery based on threefold interpenetrating network. *Adv. Mater.* **28**, 2409–2416 (2016). doi: 10.1002/adma.201505943; pmid: 26810919
26. M. Mathew, T. Schilling, M. Oettel, Connectivity percolation in suspensions of hard platelets. *Phys. Rev. E* **85**, 061407 (2012). doi: 10.1103/PhysRevE.85.061407; pmid: 23005096
27. Y. S. Hu *et al*., Synthesis of hierarchically porous carbon monoliths with highly ordered microstructure and their application in rechargeable lithium batteries with high-rate capability. *Adv. Funct. Mater.* **17**, 1873–1878 (2007). doi: 10.1002/adfm.200601152
28. P. Oh *et al*., Superior long-term energy retention and volumetric energy density for Li-rich cathode materials. *Nano Lett.* **14**, 5965–5972 (2014). doi: 10.1021/nl502980k; pmid: 25180657
29. S. Lee, Y. Cho, H.-K. Song, K. T. Lee, J. Cho, Carbon-coated single-crystal $LiMn_2O_4$ nanoparticle clusters as cathode material for high-energy and high-power lithium-ion batteries. *Angew. Chem. Int. Ed.* **51**, 8748–8752 (2012). doi: 10.1002/anie.201203581; pmid: 22865641
30. H. Gao, W. Zhou, K. Park, J. B. Goodenough, A sodium-ion battery with a low-cost cross-linked gel-polymer electrolyte. *Adv. Energy Mater.* **6**, 1600467 (2016).
31. F. Han, T. Gao, Y. Zhu, K. J. Gaskell, C. Wang, A battery made from a single material. *Adv. Mater.* **27**, 3473–3483 (2015). doi: 10.1002/adma.201500180; pmid: 25925023
32. M. Gaberscek, R. Dominko, J. Jamnik, Is small particle size more important than carbon coating? An example study on LiFePO4 cathodes. *Electrochem. Commun.* **9**, 2778–2783 (2007). doi: 10.1016/j.elecom.2007.09.020
33. Y. G. Guo, Y. S. Hu, W. Sigle, J. Maier, Superior electrode performance of nanostructured mesoporous TiO_2 (anatase) through efficient hierarchical mixed conducting networks. *Adv. Mater.* **19**, 2087–2091 (2007). doi: 10.1002/adma.200602828
34. Y. S. Hu *et al*., Improved electrode performance of porous $LiFePO_4$ using RuO_2 as an oxidic nanoscale interconnect. *Adv. Mater.* **19**, 1963–1966 (2007). doi: 10.1002/adma.200700697
35. W. M. Zhang *et al*., Tin nanoparticles encapsulated in elastic hollow carbon spheres for high-performance anode material in lithium-ion batteries. *Adv. Mater.* **20**, 1160–1165 (2008). doi: 10.1002/adma.200701364
36. N. Liu *et al*., A pomegranate-inspired nanoscale design for large-volume-change lithium battery anodes. *Nat. Nanotechnol.* **9**, 187–192 (2014). doi: 10.1038/nnano.2014.6; pmid: 24531496
37. H. Wu *et al*., Stable cycling of double-walled silicon nanotube battery anodes through solid-electrolyte interphase control. *Nat. Nanotechnol.* **7**, 310–315 (2012). doi: 10.1038/nnano.2012.35; pmid: 22447161
38. F.-F. Cao *et al*., Symbiotic coaxial nanocables: Facile synthesis and an efficient and elegant morphological solution to the lithium storage problem. *Chem. Mater.* **22**, 1908–1914 (2010). doi: 10.1021/cm9036742
39. F. Wu, J. T. Lee, E. Zhao, B. Zhang, G. Yushin, Graphene–Li_2S–carbon nanocomposite for lithium–sulfur batteries. *ACS Nano* **10**, 1333–1340 (2016). doi: 10.1021/acsnano.5b06716; pmid: 26647225
40. Y. Gong *et al*., A bottom-up approach to build 3D architectures from nanosheets for superior lithium storage. *Adv. Funct. Mater.* **24**, 125–130 (2014). doi: 10.1002/adfm.201300844
41. P. L. Taberna, S. Mitra, P. Poizot, P. Simon, J. M. Tarascon, High rate capabilities Fe_3O_4-based Cu nano-architectured electrodes for lithium-ion battery applications. *Nat. Mater.* **5**, 567–573 (2006). doi: 10.1038/nmat1672; pmid: 16783360
42. C. Zhu, X. Mu, P. A. van Aken, Y. Yu, J. Maier, Single-layered ultrasmall nanoplates of MoS_2 embedded in carbon nanofibers with excellent electrochemical performance for lithium and sodium storage. *Angew. Chem. Int. Ed.* **53**, 2152–2156 (2014). doi: 10.1002/anie.201308354; pmid: 24446245
43. Y. Yu, L. Gu, C. Zhu, P. A. van Aken, J. Maier, Tin nanoparticles encapsulated in porous multichannel carbon microtubes: Preparation by single-nozzle electrospinning and application as anode material for high-performance Li-based batteries. *J. Am. Chem. Soc.* **131**, 15984–15985 (2009). doi: 10.1021/ja906261c; pmid: 19886691
44. Y. Tang, Y. Zhang, W. Li, B. Ma, X. Chen, Rational material design for ultrafast rechargeable lithium-ion batteries. *Chem. Soc. Rev.* **44**, 5926–5940 (2015). doi: 10.1039/C4CS00442F; pmid: 25857819
45. Q. Zhao *et al*., Sulfur nanodots electrodeposited on Ni foam as high-performance cathode for Li-S batteries. *Nano Lett.* **15**, 721–726 (2015). doi: 10.1021/nl504263m; pmid: 25541748
46. T. H. Hwang, Y. M. Lee, B.-S. Kong, J.-S. Seo, J. W. Choi, Electrospun core-shell fibers for robust silicon nanoparticle-based lithium ion battery anodes. *Nano Lett.* **12**, 802–807 (2012). doi: 10.1021/nl203817r; pmid: 22206272
47. B. Liu *et al*., Hierarchical three-dimensional $ZnCo_2O_4$ nanowire arrays/carbon cloth anodes for a novel class of high-performance flexible lithium-ion batteries. *Nano Lett.* **12**, 3005–3011 (2012). doi: 10.1021/nl300794f; pmid: 22607457
48. C. Wu *et al*., Peapod-like carbon-encapsulated cobalt chalcogenide nanowires as cycle-stable and high-rate materials for sodium-ion anodes. *Adv. Mater.* **28**, 7276–7283 (2016). doi: 10.1002/adma.201600964; pmid: 27276583
49. E. Hosono, T. Kudo, I. Honma, H. Matsuda, H. Zhou, Synthesis of single crystalline spinel $LiMn_2O_4$ nanowires for a lithium ion battery with high power density. *Nano Lett.* **9**, 1045–1051 (2009). doi: 10.1021/nl803394v; pmid: 19209916
50. J. Sun *et al*., A phosphorene-graphene hybrid material as a high-capacity anode for sodium-ion batteries. *Nat. Nanotechnol.* **10**, 980–985 (2015). doi: 10.1038/nnano.2015.194; pmid: 26344183
51. Y. Yan, Y.-X. Yin, Y.-G. Guo, L.-J. Wan, A sandwich-like hierarchically porous carbon/graphene composite as a high-performance anode material for sodium-ion batteries. *Adv. Energy Mater.* **4**, 1301584 (2014). doi: 10.1002/aenm.201301584
52. W. Li *et al*., General strategy to synthesize uniform mesoporous TiO_2/graphene/mesoporous TiO_2 sandwich-like nanosheets for highly reversible lithium storage. *Nano Lett.* **15**, 2186–2193 (2015). doi: 10.1021/acs.nanolett.5b00291; pmid: 25705819
53. N. Li, S. Jin, Q. Liao, H. Cui, C. X. Wang, Encapsulated within graphene shell silicon nanoparticles anchored on vertically aligned graphene trees as lithium ion battery anodes. *Nano Energy* **5**, 105–115 (2014). doi: 10.1016/j.nanoen.2014.02.011
54. J. Liu *et al*., Graphene sandwiched mesostructured Li-ion battery electrodes. *Adv. Mater.* **28**, 7696–7702 (2016). doi: 10.1002/adma.201600829; pmid: 27383465
55. C. Liu *et al*., An all-in-one nanopore battery array. *Nat. Nanotechnol.* **9**, 1031–1039 (2014). doi: 10.1038/nnano.2014.247; pmid: 25383515
56. C. Zhu, K. Song, P. A. van Aken, J. Maier, Y. Yu, Carbon-coated $Na_3V_2(PO_4)_3$ embedded in porous carbon matrix: An ultrafast Na-storage cathode with the potential of outperforming Li cathodes. *Nano Lett.* **14**, 2175–2180 (2014). doi: 10.1021/nl500548a; pmid: 24678829
57. X.-Y. Yu, H. B. Wu, L. Yu, F.-X. Ma, X. W. Lou, Rutile TiO_2 submicroboxes with superior lithium storage properties. *Angew. Chem. Int. Ed.* **54**, 4001–4004 (2015). doi: 10.1002/anie.201411353; pmid: 25651520
58. F. Jiao, J. Bao, A. H. Hill, P. G. Bruce, Synthesis of ordered mesoporous Li-Mn-O spinel as a positive electrode for rechargeable lithium batteries. *Angew. Chem. Int. Ed.* **47**, 9711–9716 (2008). doi: 10.1002/anie.200803431; pmid: 18989873
59. H. Zhang, X. Yu, P. V. Braun, Three-dimensional bicontinuous ultrafast-charge and -discharge bulk battery electrodes. *Nat. Nanotechnol.* **6**, 277–281 (2011). doi: 10.1038/nnano.2011.38; pmid: 21423184
60. Y. You *et al*., Subzero-temperature cathode for a sodium-ion battery. *Adv. Mater.* **28**, 7243–7248 (2016). doi: 10.1002/adma.201600846; pmid: 27305570
61. Y.-K. Sun *et al*., Nanostructured high-energy cathode materials for advanced lithium batteries. *Nat. Mater.* **11**, 942–947 (2012). doi: 10.1038/nmat3435; pmid: 23042415
62. C. Yuan, H. B. Wu, Y. Xie, X. W. Lou, Mixed transition-metal oxides: Design, synthesis, and energy-related applications. *Angew. Chem. Int. Ed.* **53**, 1488–1504 (2014). doi: 10.1002/anie.201303971; pmid: 24382683
63. J. Qi *et al*., Multi-shelled hollow micro-/nanostructures. *Chem. Soc. Rev.* **44**, 6749–6773 (2015). doi: 10.1039/C5CS00344J; pmid: 26135708
64. K. Chen, S. Song, F. Liu, D. Xue, Structural design of graphene for use in electrochemical energy storage devices. *Chem. Soc. Rev.* **44**, 6230–6257 (2015). doi: 10.1039/C5CS00147A; pmid: 26051987
65. D. Li, Y. Xia, Electrospinning of nanofibers: Reinventing the wheel? *Adv. Mater.* **16**, 1151–1170 (2004). doi: 10.1002/adma.200400719
66. C. Zhu, Y. Wen, P. A. van Aken, J. Maier, Y. Yu, High lithium storage performance of FeS nanodots in porous graphitic carbon nanowires. *Adv. Funct. Mater.* **25**, 2335–2342 (2015). doi: 10.1002/adfm.201404468
67. X. Li, C. Wang, Engineering nanostructured anodes via electrostatic spray deposition for high performance lithium ion battery application. *J. Mater. Chem. A Mater. Energy Sustain.* **1**, 165–182 (2013). doi: 10.1039/C2TA00437B
68. C. Zhu, X. Mu, P. A. van Aken, J. Maier, Y. Yu, Fast Li storage in MoS_2-graphene-carbon nanotube nanocomposites: Advantageous functional integration of 0D, 1D, and 2D nanostructures. *Adv. Energy Mater.* **5**, 1401170 (2015). doi: 10.1002/aenm.201401170
69. L. Wen, M. Zhou, C. Wang, Y. Mi, Y. Lei, Nanoengineering energy conversion and storage devices via atomic layer deposition. *Adv. Energy Mater.* **6**, 1600468 (2016). doi: 10.1002/aenm.201600468
70. X. Meng, X. Q. Yang, X. Sun, Emerging applications of atomic layer deposition for lithium-ion battery studies. *Adv. Mater.* **24**, 3589–3615 (2012). doi: 10.1002/adma.201200397; pmid: 22700328
71. P. P. R. M. L. Harks, F. M. Mulder, P. H. L. Notten, In situ methods for Li-ion battery research: A review of recent developments. *J. Power Sources* **288**, 92–105 (2015). doi: 10.1016/j.jpowsour.2015.04.084
72. C. P. Grey, J. M. Tarascon, Sustainability and in situ monitoring in battery development. *Nat. Mater.* **16**, 45–56 (2016). doi: 10.1038/nmat4777; pmid: 27994251
73. N. Xu *et al*., Greatly suppressed shuttle effect for improved lithium sulfur battery performance through short chain intermediates. *Nano Lett.* **17**, 538–543 (2017). doi: 10.1021/acs.nanolett.6b04610; pmid: 27977209
74. M. Sathiya *et al*., Electron paramagnetic resonance imaging for real-time monitoring of Li-ion batteries. *Nat. Commun.* **6**, 6276 (2015). doi: 10.1038/ncomms7276; pmid: 25662295
75. S. Chandrashekar *et al*., 7Li MRI of Li batteries reveals location of microstructural lithium. *Nat. Mater.* **11**, 311–315 (2012). doi: 10.1038/nmat3246; pmid: 22327745
76. J. Wang, Y. C. Chen-Wiegart, J. Wang, In situ three-dimensional synchrotron X-Ray nanotomography of the (de) lithiation processes in tin anodes. *Angew. Chem. Int. Ed.* **53**, 4460–4464 (2014). doi: 10.1002/anie.201310402; pmid: 24648150
77. D. X. Liu *et al*., In situ quantification and visualization of lithium transport with neutrons. *Angew. Chem. Int. Ed.* **53**, 9498–9502 (2014). doi: 10.1002/anie.201404197; pmid: 25044527
78. K. Yamamoto *et al*., Dynamic visualization of the electric potential in an all-solid-state rechargeable lithium battery. *Angew. Chem. Int. Ed.* **49**, 4414–4417 (2010). doi: 10.1002/anie.200907319; pmid: 20468017
79. D. J. Miller, C. Proff, J. G. Wen, D. P. Abraham, J. Bareño, Observation of microstructural evolution in Li battery cathode oxide particles by in situ electron microscopy. *Adv. Energy Mater.* **3**, 1098–1103 (2013). doi: 10.1002/aenm.201300015
80. M. Gu *et al*., Demonstration of an electrochemical liquid cell for operando transmission electron microscopy observation of the lithiation/delithiation behavior of Si nanowire battery anodes. *Nano Lett.* **13**, 6106–6112 (2013). doi: 10.1021/nl403402q; pmid: 24224495
81. M. Hess, T. Sasaki, C. Villevieille, P. Novák, Combined operando x-ray diffraction-electrochemical impedance spectroscopy detecting solid solution reactions of $LiFePO_4$ in batteries. *Nat. Commun.* **6**, 8169 (2015). doi: 10.1038/ncomms9169; pmid: 26345306

82. X. Zhang *et al*., Rate-induced solubility and suppression of the first-order phase transition in olivine $LiFePO_4$. *Nano Lett.* **14**, 2279–2285 (2014). doi: 10.1021/nl404285y; pmid: 24707878
83. H. Liu *et al*., Capturing metastable structures during high-rate cycling of $LiFePO_4$ nanoparticle electrodes. *Science* **344**, 1252817 (2014). doi: 10.1126/science.1252817
84. J. Lim *et al*., Origin and hysteresis of lithium compositional spatiodynamics within battery primary particles. *Science* **353**, 566–571 (2016). doi: 10.1126/science.aaf4914; pmid: 27493180
85. J. Niu *et al*., In situ observation of random solid solution zone in $LiFePO_4$ electrode. *Nano Lett.* **14**, 4005–4010 (2014). doi: 10.1021/nl501415b; pmid: 24823479
86. O. Pecher, J. Carretero-Gonzalez, K. J. Griffith, C. P. Grey, Materials' methods: NMR in battery research. *Chem. Mater.* **29**, 213–242 (2017). doi: 10.1021/acs.chemmater.6b03183
87. A. Ulvestad *et al*., Topological defect dynamics in operando battery nanoparticles. *Science* **348**, 1344–1347 (2015). doi: 10.1126/science.aaa1313; pmid: 26089511
88. N. Ohmer *et al*., Phase evolution in single-crystalline $LiFePO_4$ followed by in situ scanning x-ray microscopy of a micrometre-sized battery. *Nat. Commun.* **6**, 6045 (2015). doi: 10.1038/ncomms7045; pmid: 25599854
89. W. C. Chueh *et al*., Intercalation pathway in many-particle $LiFePO_4$ electrode revealed by nanoscale state-of-charge mapping. *Nano Lett.* **13**, 866–872 (2013). doi: 10.1021/nl3031899; pmid: 23362838
90. M. Ebner, F. Marone, M. Stampanoni, V. Wood, Visualization and quantification of electrochemical and mechanical degradation in Li ion batteries. *Science* **342**, 716–720 (2013). doi: 10.1126/science.1241882; pmid: 24136360
91. F. Sun *et al*., Three-dimensional visualization of gas evolution and channel formation inside a lithium-ion battery. *ACS Appl. Mater. Interfaces* **8**, 7156–7164 (2016). doi: 10.1021/acsami.6b00708; pmid: 26926360
92. M. Ebner, F. Geldmacher, F. Marone, M. Stampanoni, V. Wood, X-ray tomography of porous, transition metal oxide based lithium ion battery electrodes. *Adv. Energy Mater.* **3**, 845–850 (2013). doi: 10.1002/aenm.201200932
93. J. Wang, Y. C. Karen Chen-Wiegart, C. Eng, Q. Shen, J. Wang, Visualization of anisotropic-isotropic phase transformation dynamics in battery electrode particles. *Nat. Commun.* **7**, 12372 (2016). pmid: 27516044
94. J. Y. Huang *et al*., In situ observation of the electrochemical lithiation of a single SnO_2 nanowire electrode. *Science* **330**, 1515–1520 (2010). doi: 10.1126/science.1195628; pmid: 21148385
95. W.-J. Yu *et al*., Lithiation of silicon nanoparticles confined in carbon nanotubes. *ACS Nano* **9**, 5063–5071 (2015). doi: 10.1021/acsnano.5b00157; pmid: 25869474
96. E. Strelcov, J. Cothren, D. Leonard, A. Y. Borisevich, A. Kolmakov, In situ SEM study of lithium intercalation in individual V_2O_5 nanowires. *Nanoscale* **7**, 3022–3027 (2015). doi: 10.1039/C4NR06767C; pmid: 25600354
97. R. Bhattacharyya *et al*., In situ NMR observation of the formation of metallic lithium microstructures in lithium batteries. *Nat. Mater.* **9**, 504–510 (2010). doi: 10.1038/nmat2764; pmid: 20473288
98. R. Amin, J. Maier, P. Balaya, D. P. Chen, C. T. Lin, Ionic and electronic transport in single crystalline $LiFePO_4$ grown by optical floating zone technique. *Solid State Ion.* **179**, 1683–1687 (2008). doi: 10.1016/j.ssi.2008.01.079
99. M. Park, X. Zhang, M. Chung, G. B. Less, A. M. Sastry, A review of conduction phenomena in Li-ion batteries. *J. Power Sources* **195**, 7904–7929 (2010). doi: 10.1016/j.jpowsour.2010.06.060
100. R. Amin, I. Belharouk, Part I: Electronic and ionic transport properties of the ordered and disordered $LiNi_{0.5}Mn_{1.5}O_4$ spinel cathode. *J. Power Sources* **348**, 311–317 (2017). doi: 10.1016/j.jpowsour.2017.02.071
101. J. P. Cho, H. S. Jung, Y. C. Park, G. B. Kim, H. S. Lim, Electrochemical properties and thermal stability of $Li_aNi_{1-x}Co_xO_2$ cathode materials. *J. Electrochem. Soc.* **147**, 15–20 (2000). doi: 10.1149/1.1393137
102. C. Ho, I. D. Raistrick, R. A. Huggins, Application of AC techniques to the study of lithium diffusion in tungsten trioxide thin-films. *J. Electrochem. Soc.* **127**, 343–350 (1980). doi: 10.1149/1.2129668
103. J. O. Besenhard *et al*., Kinetics of Li insertion into polycrystalline and nanocrystalline 'SnSb' alloys investigated by transient and steady state techniques. *J. Power Sources* **81–82**, 268–272 (1999). doi: 10.1016/S0378-7753(99)00199-8
104. N. A. Kaskhedikar, J. Maier, Lithium storage in carbon nanostructures. *Adv. Mater.* **21**, 2664–2680 (2009). doi: 10.1002/adma.200901079
105. C. K. Huang, S. Crouchbaker, R. A. Huggins, Lithium insertion in several molybdenum(IV) oxide phases at room-temperature. *J. Electrochem. Soc.* **135**, 408–412 (1988). doi: 10.1149/1.2095628
106. R. A. Huggins, in *Handbook of Battery Materials* (Wiley-VCH Verlag GmbH & Co. KGaA, 2011), pp. 405–431.

ACKNOWLEDGMENTS

The authors thank M. Kühne for useful comments on the manuscript. This work was financially supported by the Max Planck Society and the Alexander von Humboldt Foundation (Sofja Kovalevskaja award).

10.1126/science.aao2808

Science

The nanoscale circuitry of battery electrodes

Changbao Zhu, Robert E. Usiskin, Yan Yu and Joachim Maier

Science **358** (6369), eaao2808.
DOI: 10.1126/science.aao2808

Wired for success

Although overall battery performance is limited by the electrochemistry of the component materials, the actual performance can be limited by a number of factors. Zhu *et al.* review different electrode architectures for lithium-ion batteries. In particular, they look at the relations between the kinetics and dimensionality of the different electrode constituents. Making things smaller can improve transport of electrons and ions, but at the cost of making the overall architecture more complex. The authors discuss the overall design rules and criteria to guide battery design.

Science, this issue p. eaao2808